Comparison of numerical simulation results with experimental current density and methanol-crossover data for direct methanol fuel cells

Johan Ko, Giyong Lee, Yongjun Choi, Purushothama Chippar, Kyungmun Kang, Hyunchul Ju*

School of Mechanical Engineering, Inha University, 253 Yonghyun-Dong, Nam-Gu Incheon 402-751, Republic of Korea

ABSTRACT

The simulation results of a one-dimensional (1D) direct methanol fuel cell (DMFC) model are compared with the current density and methanol-crossover data that are experimentally measured under several different cell designs and operating conditions. No fitting parameters are employed for the comparison and model input parameters obtained from the literature are consistently used for all the cases of comparison. The numerical predictions agree well with the experimental data and the 1D DMFC model successfully captures key experimental trends that are observed in the cell current density and methanol-crossover data. This clearly illustrates that the present DMFC model can be applicable for optimizing DMFC component designs and operating conditions. In addition, the model simulations further indicate that the reduction of the methanol concentration in the anode catalyst layer is critical to simultaneously suppress both the electro-osmotic drag (EOD) and the diffusion aspects of methanol crossover.

© 2010 Elsevier B.V. All rights reserved.

1. Introduction

Within the last decade, portable electronic devices such as mobile phones, portable cameras, and notebook computers have become increasingly miniaturized and multi-functionalized, which generates an enormous demand for superior capacity rechargeable batteries to power these devices. As a result, the use of these mobile electronic devices has been limited by battery performance that suffers from short operation times and long recharge times. In this context, direct methanol fuel cells (DMFCs) using polymer electrolyte membranes have received considerable attention for replacing batteries for portable electronics devices due to their potentially higher energy specific and nearly zero recharge time.

Although substantial efforts have been made to advance DMFC technologies, there still exist several issues that currently prevent the appearance of DMFCs in the market. These are related to the low activity of electrocatalysts for the methanol oxidation reaction (MOR) at the anode, substantial methanol crossover from the anode to the cathode, and water imbalance between the anode and the cathode (the requirement for anode water and the flooding of cathode water). Furthermore, to exceed the energy specific of Li-ion batteries, it is necessary to feed highly concentrated methanol fuel directly into a DMFC stack; this worsens the methanol crossover problem and renders water management in DMFCs even more difficult [1].

An implication of the above observations is that DFMC component design, in terms of physical dimensions, materials, etc., is extremely important to suppress methanol crossover from the anode to the cathode. Therefore, many researchers have attempted to measure experimentally the degree of methanol crossover under various DMFC conditions and its effects on DMFC performance. Heinzel and Barragan [2] comprehensively reviewed the main features of methanol transfer through Nafion® and other types of membranes in DMFCs. They summarized the influence of various DMFC designs and operating factors such as methanol concentration, pressure, temperature, membrane thickness and catalyst morphology on methanol crossover and the resulting cell performance. Ren et al. [3] studied the effects of methanol crossover under different membrane thicknesses and temperatures. They measured methanol permeation rates across Nafion® 112, 115 and 117 membranes and found that the methanol flux rate increases with temperature. Hikita et al. [4] estimated the amount of methanol crossover by measuring the species composition in the cathode exhaust gas under different methanol feed concentrations (3, 6 and 9 vol. %) and membrane thicknesses (Nafion® 112, 115 and 117). They found that the use of a thicker membrane successfully lowers the methanol crossover flux but it also lowers the cell performance due to the larger ohmic resistance. Ravikumar and Shukla [5] demonstrated that the cathode polarization loss increases considerably with cell temperature and methanol feed concentration due to the enhanced methanol crossover. Wang et al. [6] experimentally estimated the methanol crossover rates and found that methanol crossover results in a mixed potential and poisoning of Pt catalysts that significantly increases the polarization loss on the cathode.

* Corresponding author. Tel.: +82 32 860 7312; fax: +82 32 868 1716.
E-mail address: hcju@inha.ac.kr (H. Ju).

Nomenclature

c	molar concentration, mol m^{-3}
D	diffusivity, m^2 s^{-1}
F	Faraday's constant, 96487 C mol^{-1}
I	current density, mA cm^{-1}
i_0^{ref}	reference exchange current density, mA cm^{-1}
K	absolute permeability of porous media, m^2
K_{mem}	membrane hydraulic permeability, m^2
K_{reac}	reaction rate, s^{-1}
M	molar mass, kg mol^{-1}
N	molar flux, mol m^{-2} s^{-1}
n_d	electro-osmotic drag coefficient
P	pressure, Pa
R	universal gas constant, 8.314 J mol^{-1} K^{-1}
r	pore radii, m
R_{cont}	contact resistance, mΩ cm^{-1}
s	liquid water saturation
T	operating temperature, K
U^o	standard equilibrium potential, V
V_{cell}	cell voltage, V

Shortcuts

aCL	anode catalyst layer
BL	backing layer
cCL	cathode catalyst layer
CCM	catalyst-coated membrane
MEA	membrane electrode assembly
MEM	membrane

Superscripts

cons	consumption
diff	diffusion
eff	effective
EOD	electro-osmotic drag
g	gas
l	liquid
prod	production

Subscripts

a	anode
BC	boundary condition
c	cathode
CO$_2$	carbon dioxide
in	inlet
k	species phase
mem	membrane
M	methanol
O$_2$	oxygen
ref	reference
t	total
W	water
xover	crossover

Greek symbols

γ	reaction symmetry
δ	thickness, m
ε	porosity
η	efficiency
θ	contact angle, $^\circ$
κ	proton conductivity
λ	water content
μ	viscosity, kg cm^{-1} s^{-1}
ξ	stoichiometric ratio

ρ	density, kg m^{-3}
σ	surface tension, N m^{-1}
τ	tortuosity

As mentioned above, it has been experimentally proven that methanol crossover is a key issue in DMFCs and that there are a number of design and operating parameters that influence the degree of methanol crossover and the resulting cell performance. That indicates that a DMFC demands a high degree of optimization. For the successful design and operation of a DMFC system, a better understanding of methanol-crossover phenomena is essential and can most likely be achieved by theoretical DMFC modeling, as well as experimental investigations.

A number of DMFC models have been developed for the purpose of obtaining a basic understanding of key physical phenomena in DMFCs and optimizing cell designs and operating conditions. These DMFC models range from simple one-dimensional mathematical models [7–12] to complex multi-dimensional, CFD models [13–18]. Despite the fact that rapid advances in DMFC modeling in the last decade have yielded substantial predictive capabilities, efforts for model validation against experimental data have been relatively limited to quite a narrow range of DMFC operating conditions.

Scott et al. [7] developed a single-phase, semi-empirical 1D DMFC model and investigated the impact of methanol crossover on cell performance. In their study, the results of the simulation model were compared with experimental data that were measured under the operating conditions of a methanol feed concentration of 1 M at the anode and three values of the oxygen pressure on the cathode (1, 2 and 3 bars). They reported good agreement between the model calculations and experimental data only over a range of moderate current densities (350–400 mA cm^{-2}); considerable deviations occur at low and high current densities. Murgia et al. [8] developed a one-dimensional, two-phase model for a liquid-feed DMFC and intensively studied methanol-crossover phenomena with different methanol feed concentrations and membranes. They successfully validated their model against the experimental data measured by Hikita et al. [4] under various methanol feed concentrations (0.5, 1.0, 1.5 M). In the model validation, however, several key parameters related to water flooding and condensation/evaporation were considered to be adjustable parameters for a better fit with the experimental data. Chen and Zhao [9] developed a ID, non-isothermal DMFC model and investigated thermal effects on methanol crossover and cell performance. They did not, however, attempt to experimentally validate their model. Recently, Kareemulla and Jayanti [10] introduced a ID, single-phase DMFC model and studied the limiting current density and methanol-crossover phenomena in DMFCs. They decomposed the methanol crossover flux into electro-osmotic and diffusion-driven methanol fluxes and intensively analyzed the behaviour of methanol crossover over a wide range of methanol feed concentrations (0.125–5.0 M). Their model validation, however, was conducted under a narrow range of methanol feed concentrations, i.e., 0.125, 0.25 and 0.5 M. Oliveira et al. [11] presented a one-dimensional, single-phase DMFC model and precisely studied methanol crossover and water transport across the membrane. They compared simulation results with experimental data that were measured at low methanol feed concentrations (0.1, 0.2, and 0.5 M) and a fixed temperature, viz., 70 °C. Eccarius et al. [12] formulated a one-dimensional methanol crossover model to describe methanol crossover from the anode to the cathode. The model calculation results were compared with methanol crossover current density data that were measured under various methanol feed concentrations, temperatures, and membrane thicknesses.

In their work, however, the electro-osmotic drag (EOD) coefficient and the methanol concentration in the cathode catalyst layer were adjustable parameters for fitting with the experimental data.

Multi-dimensional DMFC models have been presented by many DMFC modeling groups. Wang and Wang [13] presented a 2D, two-phase mixture model for a liquid-feed DMFC. The model predictions were compared with experimental data that were obtained from a 5 cm² cell under various operating conditions (1 and 2 M methanol concentrations; 50 and 80 °C operating temperatures; different anode and cathode flow rates). Divisek et al. [14] developed a 2D, two-phase DMFC model in which the effects of both oxygen and methanol electrochemical kinetics and methanol permeation across the membrane were considered. Their model was experimentally validated under various methanol feed concentrations (0.5, 1 and 2 M) at a fixed temperature of 85 °C. Yang and Zhao [15] developed a 2D, isothermal, two-phase DMFC model. They adopted classical multi-phase theory based on Darcy's law to describe two-phase transport in the anode and cathode porous regions and utilized the drift-flux and homogeneous mist-flow models for the anode and cathode flow channels, respectively. In addition, an agglomerate model was used to model oxygen transport in the catalyst layer for the oxygen reduction reaction (ORR). The model was validated against experimental data that were collected under various methanol feed concentrations (0.25, 0.5, 1.0 and 2.0 M). He et al. [16] developed a 2D, two-phase DMFC model and compared the model predictions with experimental data for the 1 M methanol feed concentration and an operating temperature of 70 °C. Ge and Liu [17] developed a two-phase, isothermal, 3D DMFC model and analyzed mainly the effects of anode carbon dioxide blockage and cathode flooding. Their model was experimentally validated at a methanol feed concentration of 1 M and a cell temperature of 70 °C. Saarinen et al. [18] produced a 3D, single-phase DMFC model and applied it to real-scale DMFC geometries. The simulation results were compared with current-density distribution data that were measured with a segmented cell. In their model validation, however, they adjusted the methanol oxidation rate at the cathode catalyst layer to fit with the experimental data.

The majority of the aforementioned DMFC models are primarily focused on methanol crossover. To date, most of the DMFC model validations have been done only against experimental data that were under a narrow range of operating conditions, particularly, in terms of the methanol feed concentration. Furthermore, few DMFC models have been directly compared with experimental data that are related to methanol crossover, even if plenty of methanol-crossover data are available in the literature. Therefore, the purpose of this study is to present a comprehensive comparison between numerical simulation results and experimental data, using a 1D DMFC model that was developed earlier [19,20]. For comparison, the experiment was performed with reference to a unit cell of 25 cm²; further, current-density measurements were made under various methanol feed concentrations and operating temperatures. In addition, 1D simulation results were compared with methanol-crossover data that were measured by Eccarius et al. [12] to examine more precisely methanol-crossover phenomena in DMFCs.

2. Experimental details

2.1. MEA fabrication

Membrane electrode assemblies (MEAs) with an active area of 25 cm² were prepared using a conventional method of fabrication based on a catalyst-coated electrode (CCE). Commercial Toray TGPH-060 (190 μm thick) was pretreated with 5 wt.% PTFE solution for the anode backing layer. On the other hand, Sigracet 25BC (235 μm thick, 40 wt.% PTFE) was used for the cathode backing layer. Carbon-supported PtRu (Hispec 12100, Johnson Matthey®) and carbon-supported Pt (Hispec 13100, Johnson Matthey®) were used for the anode and cathode catalysts, respectively. To prepare the catalyst slurry, the catalysts were mixed with 5 wt.% Nafion® solution (EW 1100, Aldrich), de-ionized (DI) water, and isopropyl alcohol. After sonication for 10 min, the catalyst slurry was brushed uniformly on the backing layers. The catalyst loading for both the anode and cathode was 2 mg cm⁻². Nafion® 115 membranes (EW 1100) from DuPont were employed on all the
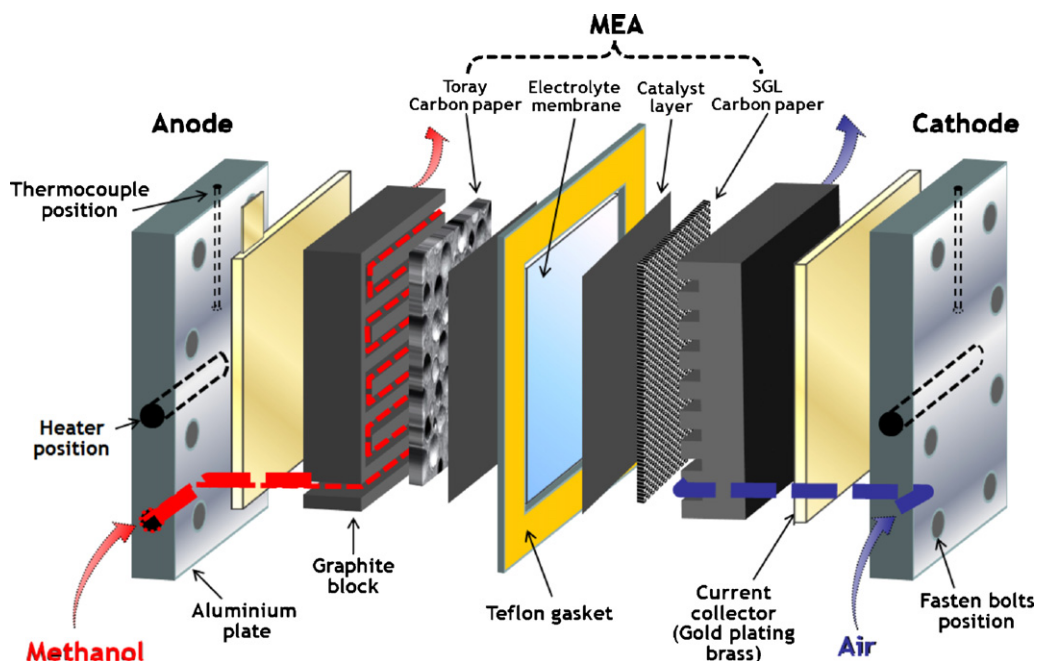

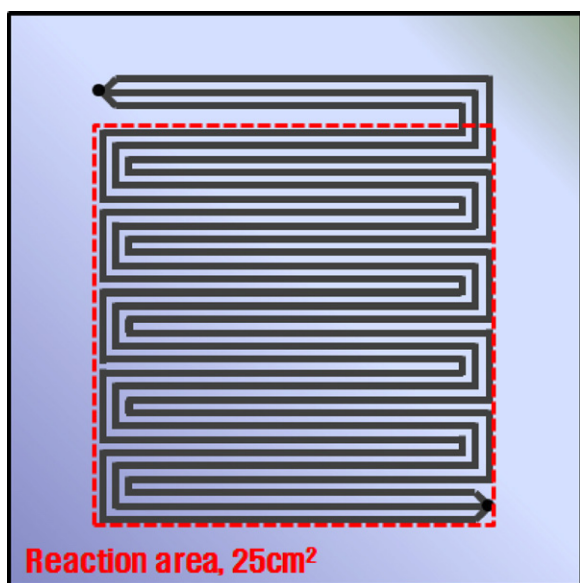**Fig. 1.** Schematic diagram of single-cell DMFC hardware.

Fig. 2. Schematic diagram of a three-path serpentine flow channel design for a 25 cm^2 test cell (channel width = 0.8 mm, channel depth = 1 mm, and land width = 0.9 mm).

experiments. The membranes were cleaned and treated by means of the following procedure. The membrane sample was dipped in hydrogen peroxide solution (H_2O_2) at 80 °C for 80 min to eliminate organic impurities and then washed with DI water. Afterwards, it was immersed in sulfuric acid (H_2SO_4) at 80 °C for 80 min to remove any metallic impurities and then again washed with DI water. The treated membrane was positioned between the catalyst-coated anode and cathode backing layers; this was followed by a hot pressing procedure at 135 °C at a pressure of 9.8 MPa for 90 s.

2.2. Cell assembly and testing

The design of the test cell is shown in Fig. 1. A MEA was sandwiched between anode and cathode graphite blocks. Two gold-coated brass plates were used as current-collectors for the anode and the cathode. The current-collectors were pressed to the graphite blocks by using end-plates made out of aluminum. Thermo-couples and electric heaters were inserted into the aluminum plates to maintain the cell operating temperature at the prescribed value. The flow channels were machined into the surface of each graphite block as shown in Fig. 2. The three-pass serpentine flow channels have width and depth of 0.8 and 1 mm, respectively.

The assembled single cell was connected to a fuel cell test station that could operate in either a constant-current or constant-voltage mode and that was able to record current–voltage data. In all experiments, a test station from Fuel Cell Technology was used to control the load, cell temperature, gas flow rate, humidity, and back-pressure. Methanol solution for the anode was supplied using a peristaltic pump (REGLO-CPF, ISMATEC) and the air flow rate for the cathode was adjusted by a mass flow controller in the fuel cell test station. The single cell was activated before each experiment as follows.

(1) Flush 1 M methanol over 12 h at the anode side (room temperature, 2 sccm), while the cathode is closed.
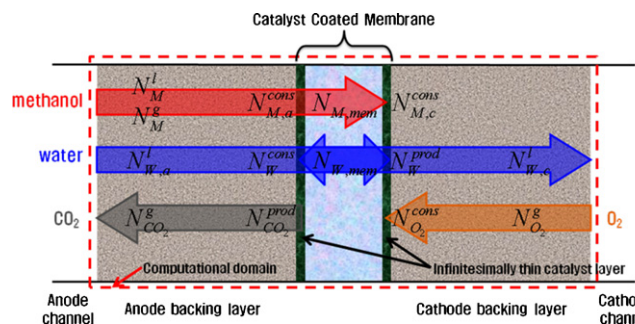(2) Feed air at the cathode side and check the open-circuit voltage (OCV) for approximately 2 h at 70 °C.

Fig. 3. Schematic of the computational domain and species transport phenomena of the 1D DMFC model.

(3) Perform a preliminary test three times in the constant-current mode at 30, 40, 50, 60, 70 and 80 °C.

After the activation procedure, polarization measurements were started at the OCV and the cell was operated in the galvanostatic mode at a scan rate of 18 mA s^{-1} for each step.

3. Model

3.1. Model description and assumptions

In this study, a two-phase, isothermal, steady-state numerical DMFC model previously developed by Ko et al. [19] is used. Fig. 3 shows the 1D computational domain of a DMFC MEA that has backing layers on both the anode and a cathode sides and catalyst-coated membrane (CCM); the detailed species transfer process is also given. The methanol that reaches the anode catalyst layer (CL) in the liquid and the gas phases dissociates into electrons and protons via the following oxidation reaction:

$$MOR : CH_3OH + H_2O \rightarrow 6H^+ + 6e^- + CO_2 \tag{1a}$$

The gas-phase oxygen passes through the cathode backing layer (BL) before reaching the cathode CL, where it reduces to water via the following reaction.

$$ORR : \ 6H^+ + 6e^- + \frac{3}{2}O_2 \rightarrow 3H_2O \tag{1b}$$
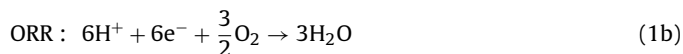
Due to the sluggish MOR reaction at the anode CL and the inherent characteristics of polymer electrolyte membranes, such as Nafion® type membranes that readily absorb water and methanol, methanol crossover is unavoidable in DMFCs. The crossed-over methanol results in an additional oxidation reaction at the cathode CL that causes a mixed-cathode overpotential and thereby reduces the fuel efficiency.

The present model invokes the following assumptions.

(1) The gas phase obeys the ideal gas law because all the gases in a DMFC are maintained under low pressure (compared with to their respective critical pressures) and high temperature (above room temperature).
(2) A temperature gradient along the cell thickness is neglected in the 1D model due to the thin MEA configuration in a DMFC.
(3) An isotropic and homogeneous porous backing layer (BL) is assumed and characterized by effective porosity and permeability.
(4) The effect of CO_2 blockage on cell performance is neglected due to lack of experimental data for the movement of CO_2 bubbles in anode BLs. In the literature, the dynamic behaviour of CO_2 bubbles has been mainly observed in anode channels which are not included in the computational domain of the present

1D DMFC model. Under this assumption, only tiny CO_2 bubbles form and travel easily through the anode BL, which results in a small fraction of carbon dioxide at the anode BL. The prediction of the real impact of CO_2 blockage on DMFC performance requires more rigorous studies that are related to the bubble detachment size/frequency and bubble surface coverage, which are beyond the scope of this work.

(5) Complete consumption of methanol at the cathode CL is assumed after it crosses over the membrane from the anode to the cathode.

(6) The electrolyte membrane is fully hydrated due to the dominant liquid phase in DMFCs. This is based on the fact that an aqueous methanol solution is supplied as the fuel at the anode side and significant flooding usually occurs at the cathode side due to the combined effects of methanol crossover and the ORR.

(7) Given that gas permeation through the electrolyte membrane is usually small in a DMFC, the effects of oxygen and carbon dioxide crossover through the membrane are neglected.

3.2. Species balance equations

Two-phase, species fluxes in the through-plane direction in the anode BL, catalyst membrane (CCM) and cathode BL can be obtained by considering the balances of individual species, i.e., methanol, water, oxygen and carbon dioxide species, which are expressed in Eqs. (2) through to (6). Here, the species flux direction from the anode to cathode is defined as the positive direction.

Methanol balance between anode BL and CCM:

$$N_M^l + N_M^g = \frac{I}{6F} + N_{M,mem} \tag{2}$$

Water balance between anode BL and CCM:

$$N_{W,a}^l = \frac{I}{6F} + N_{W,mem} \tag{3}$$

Water balance between cathode BL and CCM:

$$N_{W,c}^l = \frac{I}{2F} + 2N_{M,mem} + N_{W,mem} \tag{4}$$

Carbon dioxide balance between anode BL and CCM:

$$N_{CO_2}^g = -\frac{I}{6F} \tag{5}$$

Oxygen balance between cathode BL and CCM:

$$N_{O_2}^g = -\frac{I}{4F} - \frac{3}{2}N_{M,mem} \tag{6}$$

where, I, $N_{M,mem}$, and $N_{W,mem}$ denote the operating current density, and the methanol and water crossover fluxes through the membrane, respectively.

3.2.1. Methanol transport equation

The two-phase methanol transport in the anode BL is derived using Maxwell–Stefan's multi-component diffusion equation [21]:

$$\nabla x_\alpha = -\sum_{\beta=1}^{N} \frac{1}{cD_{\alpha\beta}}(x_\beta N_\alpha - x_\alpha N_\beta) \tag{7}$$

For a binary liquid-transport system through the porous BLs of DMFCs, the binary diffusivity, $D_{\alpha\beta}$, should be modified via the Bruggeman correlation to account for the effect of the porosity, tortuosity of the anode BL, and liquid saturation, i.e., the volume fraction of liquid that occupies the open pore space of the

anode BL. The resultant effective diffusivity can be written as follows.

$$D_M^{l,eff} = D_M^l (\varepsilon S)^n \tag{8}$$

Now, Eq. (7) can be rewritten for the binary liquid-transport system in the anode BL that includes methanol and water as follows.

$$\nabla x_M^l = \frac{x_M^l N_{w,a}^l - x_W^l N_{M,a}^l}{c_t^l D_M^{l,eff}} \tag{9}$$

In the above equation, the molar fractions of methanol and water are defined as follows.

$$x_M^l = \frac{c_M^l}{c_t^l}; \quad x_W^l = \frac{c_W^l}{c_t^l} = 1 - x_M^l \tag{10}$$

where c_t^l represents the total molar concentration of the liquid phase in the anode BL, i.e., the sum of the individual molar concentrations, namely:

$$c_t^l = c_M^l + c_W^l \tag{11}$$

Using Eqs. (10) and (11), Eq. (9) for the methanol flux through the anode BL, $N_{M,a}^l$, can be rewritten as follows.

$$N_{M,a}^l = \frac{c_M^l N_{W,a}^l - c_t^l D_M^{l,eff} \nabla c_M^l}{c_t^l - c_M^l} \tag{12}$$

The gas-phase transport in the anode BL is assumed to be a binary diffusion system that consists of methanol vapour and carbon dioxide. Again, using the Maxwell–Stefan equation, viz., Eq. (9), the molar fraction of methanol vapour can be written as:

$$\nabla x_M^g = \frac{x_M^g N_{CO_2,a}^g - x_{CO_2}^g N_{M,a}^g}{c_t^g D_M^{g,eff}} \tag{13}$$

In Eq. (13), the effective diffusivity of methanol vapour, $D_M^{g,eff}$, in the anode BL can be a function of the porosity, liquid saturation, and the Bruggeman factor, n, as follows.

$$D_M^{g,eff} = D_M^g [\varepsilon(1-s)]^n \tag{14}$$

According to the ideal gas law, the total molar concentration of gas, c_t^g, can be determined as follows.

$$c_t^g = \frac{P_a}{RT} \tag{15}$$

Now, Eq. (13) can be written for the methanol vapour flux along the anode BL, $N_{M,a}^g$, as:

$$N_{M,a}^g = \frac{c_M^g N_{CO_2,a}^g - c_t^g D_M^{g,eff} \nabla c_M^g}{c_t^g - c_M^g} \tag{16}$$

Assuming methanol and methanol vapour to be in thermodynamic equilibrium and applying Henry's law to Eq. (16), we can express the methanol vapour flux, $N_{M,a}^g$, in terms of c_M^l instead of c_M^g:

$$N_{M,a}^g = \frac{c_M^l N_{CO_2,a}^g - c_t^g D_M^{g,eff} \nabla c_M^l}{k_H c_t^g - c_M^l} \tag{17}$$

where Henry's constant, k_H, is defined as the ratio between the methanol concentration in the liquid and gas phases and is expressed as a function of temperature, i.e.,

$$k_H = \frac{c_M^l}{c_M^g} = k_H^0 e^{-(\Delta H_{sol}/R)((1/T)-1/T_0)} RT \tag{18}$$

where, k_H^0 refers to Henry's constant at the reference state of $T_0 = 298.15\,K$ and ΔH_{sol} refers to the enthalpy of the solution.

Using Eqs. (2), (3), (5), (12), and (17), it is possible to obtain the final form of the methanol balance equation between the anode BL and the membrane as follows:

$$\frac{c_M^l((I/6F) + N_{W,mem}) - c_t^l D_M^l \nabla c_M^l}{c_t^l - c_M^l} + \frac{c_M^l(-I/6F) - c_t^g D_M^g \nabla c_M^l}{k_H c_t^g - c_M^l}$$

$$= \frac{I}{6F} + N_{M,mem} \tag{19}$$

In Eq. (19), the methanol flux that passes through the membrane, $N_{M,mem}$, can be driven by the EOD due to the proton flux and diffusion that arise from the methanol concentration gradient across the membrane:

$$N_{M,mem} = N_{M,mem}^{eod} + N_{M,mem}^{diff} = n_{d,M}\frac{I}{F} + D_{M,mem}\frac{c_M^l|_{aCL}}{\delta_{mem}} \tag{20}$$

where $n_{d,M}$ denotes the EOD coefficient of methanol given by Liu [22], which is a function of the EOD coefficient of water, $n_{d,W}$, and the methanol and water concentrations in the anode catalyst layer. That is,

$$n_{d,M} = n_{d,W}\frac{c_M^l}{c_W^l}\bigg|_{aCL} \tag{21}$$

3.2.2. Oxygen-transport equation

The diffusion flux of oxygen through the cathode BL is expressed using Fick's diffusion equation. Therefore, with Eqs. (6) and (20), the final form of the oxygen transport equation for the cathode side can be obtained as follows:

$$N_{O_2}^g = D_{O_2}^{g,eff} \nabla c_{O_2}^g = -\frac{I}{4F} - \frac{3}{2}N_{M,mem}$$

$$= -(6n_{d,M} + 1)\frac{I}{4F} - \frac{3}{2}D_{M,mem}\frac{c_M^l|_{aCL}}{\delta_{mem}} \tag{22}$$

where $D_{O_2}^{g,eff}$ is the effective diffusion coefficient of oxygen through the cathode BL and is expressed as a function of the porosity, liquid saturation, and Bruggeman factor, n, as follows.

$$D_{O_2}^{g,eff} = D_{O_2}^g [\varepsilon(1 - s)]^n \tag{23}$$

3.2.3. Liquid-saturation equation

The derivation of the liquid saturation equation commences from the mass conservation equation for the liquid phase. For the anode side, the mass conservation equation for the liquid phase can be expressed as:

$$\rho^l u^l = -M_M N_{M,a}^l - M_W N_{W,a}^l \tag{24}$$

On the other hand, Darcy's law can be employed to describe liquid flow in porous media, such as the anode BL:

$$u^l = -\frac{K}{\mu^l}k_r^l \nabla P^l \tag{25}$$

where K and k_r^l denote the permeability of the given porous medium and the relative permeability for the liquid phase, respectively. The capillary pressure, P_c can be expressed as a function of the surface tension, σ, porosity, ε, permeability, K, and contact angle, θ, of the porous medium as follows [23]:

$$P_c = P^g - P^l = \sigma \cos \theta \left(\frac{\varepsilon}{K}\right)^{1/2} J(s) \tag{26}$$

where the Leverett function, $J(s)$, is the dimensionless capillary pressure, which can be expressed for both hydrophobic and hydrophilic porous layers as follows.

$$J(s) = \begin{cases} 1.417(1-s) - 2.120(1-s)^2 + 1.263(1-s)^3 & \text{if } \theta < 90° \\ 1.417s - 2.120s^2 + 1.263s^3 & \text{if } \theta > 90° \end{cases} \tag{27}$$

The liquid-phase Darcy's equation, Eq. (25), can be rewritten in terms of the capillary pressure, P_c, by assuming that the pressure drop through the gas flow is relatively negligible when compared with the gradient of the liquid pressure.

$$u^l = \frac{K}{\mu^l}k_r^l \nabla P_c = \frac{K}{\mu^l}k_r^l \frac{2\sigma \cos \theta}{r}\frac{dJ}{ds}\nabla s \tag{28}$$

By combining Eqs. (12) and (28) into Eq. (24), the final form of the liquid-transport equation at the anode can be expressed as follows:

$$\rho^l \frac{K_a}{\mu^l}k_r^l \frac{2\sigma \cdot \cos \theta}{r_a}\frac{dJ}{ds}\nabla s = -M_M \left(\frac{c_M^l N_{W,a}^l - c_t^l D_M^{l,eff}\nabla c_M^l}{c_t^l - c_M^l}\right)$$

$$- M_W N_{W,a}^l \tag{29}$$

where $N_{W,a}^l$ denotes the water flux through the anode BL. According to Eq. (3), $N_{W,a}^l$ is equivalent to the sum of the water consumption rates through the MOR at the anode side, $I/6F$, and the water flux across the membrane, $N_{W,mem}$, i.e., driven by the EOD due to the proton flux, the diffusion due to the water-content gradient, and the hydraulic pressure gradient, as shown by:

$$N_{W,mem} = N_{W,mem}^{EOD} + N_{W,mem}^{diff} - N_{W,mem}^{pl}$$

$$= n_{d,W}\frac{I}{F} + D_{W,mem}\frac{\rho_{mem}}{EW}\frac{\lambda_a - \lambda_c}{\delta_{mem}} - \frac{K_{mem}}{M_W \nu^l}\frac{P_c^l - P_a^l}{\delta_{mem}} \tag{30}$$

Similarly, we can derive the liquid-transport equation at the cathode side as follows.

$$\rho^l \frac{K_c}{\mu^l}k_r^l \frac{2\sigma \cos \theta}{r_c}\frac{dJ(s)}{ds}\nabla s = M_W \left(\frac{I}{2F} + 2N_{M,mem} + N_{W,mem}\right) \tag{31}$$

3.2.4. Electrochemical kinetics

At a given current density, I, the cell voltage is determined from the theoretical thermodynamic potential, anode and cathode overpotentials, membrane ohmic resistance, and contact resistance as follows.

$$V_{cell} = U^o - \eta_a + \eta_c - IR_{cont} - I\frac{\delta_{mem}}{\kappa_{mem}} \tag{32}$$

Regarding Eq. (32), it should be mentioned that the theoretical equilibrium potential U^o represents the difference between the anode and cathode standard potentials ($U^o = U_c^o - U_a^o$), which are respectively determined by using the Nernst equation as follows.

For the anode:

$$U_a^o = \frac{-\Delta \bar{g}_a^0}{6F} = -0.016\,\text{V} \quad \text{vs. standard hydrogen electrode (SHE)} \tag{33}$$

For the cathode:

$$U_c^o = \frac{-\Delta \bar{g}_c^o}{6F} = 1.229\,\text{V} \quad \text{vs. SHE} \tag{34}$$

The second and third terms in the right-hand side of Eq. (32) are the anode kinetic loss, η_a, and the cathode kinetic loss, η_c. These two parameters are calculated from the electrochemical kinetics expressions obtained from the Butler–Volmer equation.

For the anode MOR:

$$I = i_{o,a}^{ref} \frac{c_M|_{aCL} \exp\left((\gamma_a/RT)F\eta_a\right)}{c_M|_{aCL} + K_{reac} \exp\left((\gamma_a/RT)F\eta_a\right)} \tag{35}$$

For the cathode ORR:

$$I + I_{xover} = i_{o,c}^{ref}(1 - s_c) \left(\frac{c_{O_2}|_{cCL}}{c_{O_2}^{ref}} \right) \exp\left(\frac{\gamma_c}{RT} F\eta_c \right) \tag{36}$$

The MOR kinetic expression in Eq. (35) was derived by Meyers and Newman [24] from a four-step mechanism proposed by Gasteiger et al. [25]. In Eq. (35), $c_M|_{aCL}$ and K_{reac} stand for the methanol concentration at the anode CL and the reaction constant, respectively. On the other hand, the ORR kinetics expression in Eq. (36) is based on first-order Tafel kinetics and is obtained from the experimental studies of Bernardi and Verbrugge [26], and Gottesfeld and Zawodzinski [27]. In addition, $i_{0,a}^{ref}$ and $i_{0,c}^{ref}$ denote the exchange current densities for the anode MOR and cathode ORR, respectively, which are given by Wang and Wang [13] as follows.

For the anode MOR:

$$i_{o,a}^{ref}(T) = 94.25 \ \exp\left(\frac{35570}{R} \left(\frac{1}{353} - \frac{1}{T} \right) \right) \tag{37}$$

For the cathode ORR:

$$i_{o,c}^{ref}(T) = 0.0422 \exp\left(\frac{73200}{R} \left(\frac{1}{353} - \frac{1}{T} \right) \right) \tag{38}$$

Finally, the last two terms in Eq. (32) are related to the ohmic losses due to the contact resistance and membrane resistance, respectively. Regarding the membrane resistance, δ_{mem} and κ_{mem} stand for the membrane thickness and proton conductivity through the membrane, respectively.

3.3. Boundary conditions

The species concentrations that are applied to the anode|cathode BL|channel interfaces are calculated based on the methanol and oxygen concentrations in the anode and cathode channel inlets, respectively.

Methanol concentration for anode:

$$c_M^l|_{aBC} = c_{M,in}^l \left(1 - \frac{1}{2\xi_a} \right) \tag{39}$$

Oxygen concentration for cathode:

$$c_{O_2}^g|_{cBC} = c_{O_2,in}^g \left(1 - \frac{1}{2\xi_c} \right) \tag{40}$$

In the above, ξ_a and ξ_c represent the anode and cathode stoichiometric numbers, respectively.

On the other hand, for the liquid-transport equations, viz., Eqs. (29) and (31), the values of the interfacial liquid coverage of the anode and the cathode BL surfaces are assumed to be 0.8 and 0.1, respectively.

For the anode:

$$s|_{aBC} = 0.8 \tag{41}$$

For the cathode:

$$s|_{cBC} = 0.1 \tag{42}$$

The above assumptions are based on the fact that in DMFCs, the two-phase flow in the anode channel is more like a pure liquid flow with a small gas fraction, whereas the gas phase is usually more dominant in the two-phase flow pattern along the cathode gas channel.

3.4. Numerical procedures

The governing equations derived in the foregoing section are implemented using a FORTRAN code and solved simultaneously in the entire computational domain that comprises the anode BL, CCM, and cathode BL. After the computational domain is initialized, the methanol transport equation is first solved. Then, the cell voltage is calculated from the known current density and methanol

Table 1
Transport and physical properties.

Description	Value	Ref.
Water density, ρ_W	1.0×10^3 kg m^{-3}	[22]
Methanol density, ρ_M	0.79×10^3 kg m^{-3}	[22]
Membrane density, ρ_{mem}	1.98×10^3 kg m^{-3}	[22]
Faraday constant, F	96, 487 C mol^{-1}	[13]
Membrane equivalent weight, EW	1.1 kg mol^{-1}	[22]
Porosity of anode backing layer, ε_a	0.6	[30]
Porosity of cathode backing layer, ε_c	0.6	[30]
Cell contact resistance, R_{cont}	0.2×10^{-4} Ω m^2	Assumed
Anode BL permeability, K_{aBL}	1.0×10^{-12} m^2	[15]
Cathode BL permeability, K_{cBL}	1.0×10^{-12} m^2	[15]
Membrane permeability, K_{mem}	4.0×10^{-20} m^2	[30]
Surface tension, σ	0.0625 N m^{-1}	[16]
Proton conductivity of the membrane, κ_{mem}	$(0.5139\lambda - 0.326)\exp\left[1268\left(\frac{1}{333} - \frac{1}{T}\right)\right]$ s m^{-1}	[13]
Water viscosity, μ^l	$\begin{bmatrix} 0.458509 - 5.34047 \times 10^{-3}T+ \\ 2.31231 \times 10^{-5}T^2 - 4.49161 \times 10^{-8}T^3 \\ +3.27681 \times 10^{-11}T^4 \end{bmatrix}$ kg m^{-1} s^{-1}	[13]
Methanol diffusivity in liquid, D_M^l	$10^{-5.4163 - 999.778/T}$ m^2 s^{-1}	[13]
Methanol diffusivity in gas, D_M^g	$\begin{bmatrix} -6.954 \times 10^{-2} + 4.5986 \times 10^{-4}T \\ +9.4979 \times 10^{-7}T^2 \end{bmatrix} \times 10^{-4}$ m^2 s^{-1}	[13]
Oxygen diffusivity in gas, $D_{O_2}^g$	$1.775 \times 10^{-5} \left(\frac{T}{273}\right)^{1.823}$ m^2 s^{-1}	[13]
Methanol diffusivity in the membrane, $D_{M,mem}$	$1.98 \times 10^{-10} \ \exp\left(2416\left(\frac{1}{298} - \frac{1}{T}\right)\right)$ m^2 s^{-1}	Fitted [31]
Water diffusivity in the membrane, $D_{W,mem}$	$4.80 \times 10^{-11} \exp\left(2416\left(\frac{1}{303} - \frac{1}{T}\right)\right)$ m^2 s^{-1}	[30]
Electro-osmotic drag coefficient of water, $n_{d,W}$	$1.6767 + 0.0155 \times (T - 273) + 8.9074 \times (T - 273)^2$	Fitted [32]

crossover rate. Next, the liquid-saturation and oxygen-transport equations are solved successively. After all the transport equations are calculated, the related parameters are updated. The iterations proceed until the methanol concentration at the anode CL satisfies the convergence criterion ($<10^{-5}$).

4. Results and discussion

For the present model validation study, the polarization curve measurements were conducted using an in-house 25 cm^2 MEAs. The voltage–current density data were collected at three different cell temperatures (50, 60, and 70 °C) and four different methanol feed concentrations (1, 2, 3 and 4 M). For all experimental cases, the flow rates for the anode and cathode sides were fixed at 8 sccm for the methanol solution and 1500 sccm for air; these lead to sufficiently high stoichiometric factors for the anode and cathode flow rates (roughly 30 for both the anode and cathode sides based on 1 M methanol and dry air at the reference current density of 100 mA cm^{-2}). It should be noted that the use of a sufficiently high air flow rate in the present experiment is to prevent the generation of negative (electrolytic) current, i.e., caused by methanol crossover followed by MOR at the cathode side [28,29].

For a comparison of the results between the simulations and experiments, one-dimensional numerical simulations were carried out under the same geometric (through-plane direction) and operating conditions as in the experiments. It should be emphasized that all the input parameters listed in Table 1 were used for all the simulation cases and no adjustable parameters were considered for fitting with the experimental data.

A comparison of the calculated and measured polarization curves at three operating temperatures (50, 60 and 70 °C) for a methanol feed concentration of 1 M is given in Fig. 4. Generally, good agreement between the simulations and experiments is achieved except in the region of low current density. The deviations can be attributed to the use of the Tafel kinetic expressions, viz., Eqs. (35) and (36), and the kinetic parameters, namely, Eqs. (37) and (38). The effect of the operating temperature is seen clearly in Fig. 4. Both the calculated and the measured cell performance increase with the temperature within the 50–70 °C range. This implies that the positive effect due to the improved electrochemical kinetics and reactant transport with rising temperature is more prominent than the negative effect caused by methanol crossover that is enhanced by the rising temperature.
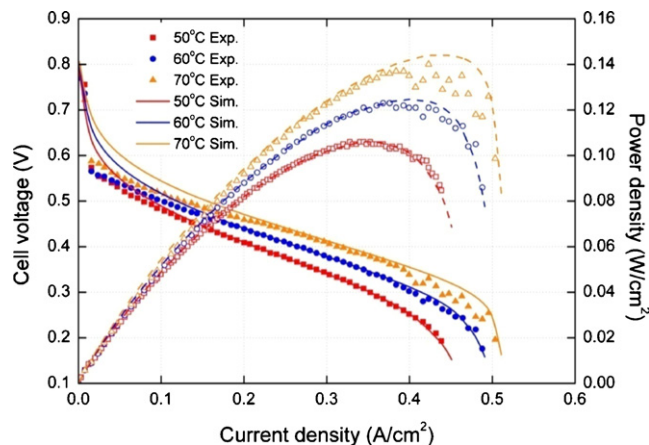

Fig. 5. Comparison of the simulated (lines) and measured (symbols) polarization curves at different cell temperatures (50, 60, and 70 °C) for a methanol concentration of 2 M.

Simulated and measured polarization curves for a methanol feed concentration of 2 M are presented in Fig. 5. Again, excellent agreement between the results of the simulations and those of the experiments is seen, although there is inadequate agreement at low current densities due to the Tafel approximation. When compared with the case of 1 M (Fig. 4), the polarization curves for 2 M (Fig. 5) reveal a reduction in the mass-transport limitation due to the use of a higher methanol feed concentration. Therefore, the limiting current densities in the cases of 2 M exist in the vicinity of 0.45–0.5 A cm^{-2}, whereas those for 1 M cases are 0.2–0.3 A cm^{-2}.

Simulated polarization curves with the experimental data for a methanol feed concentration of 3 M are given in Fig. 6. Similar to Figs. 4 and 5, good agreement between the results of the simulations and those of the experiments is observed. When compared with Fig. 5, the data in Fig. 6 clearly show that the cell performance for 3 M is slightly lower than for 2 M, which is indicative of the enhanced methanol crossover due to the raised methanol feed concentration. The results of model validation for a methanol feed concentration of 4 M are given in Fig. 7. Once again, similar to low methanol feed concentrations, by comparing the results of the simulations with those of the experiments, it is seen that the model validation is satisfactory. Nevertheless, the agreement is relatively poor at 70 °C where the model overestimates cell performance. It should be noted that the differences between the
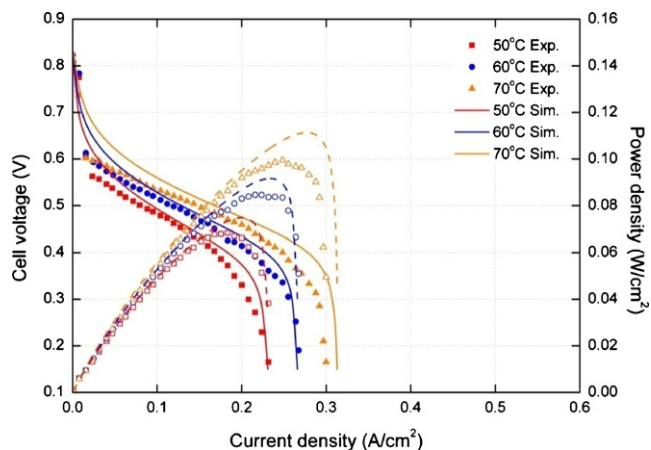

Fig. 4. Comparison of the simulated (lines) and measured (symbols) polarization curves at different cell temperatures (50, 60, and 70 °C) for a methanol concentration of 1 M.
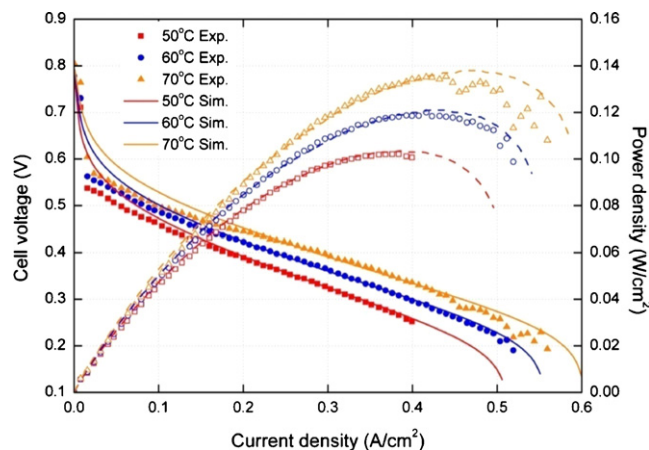

Fig. 6. Comparison of the simulated (lines) and measured (symbols) polarization curves at different cell temperatures (50, 60, and 70 °C) for a methanol concentration of 3 M.
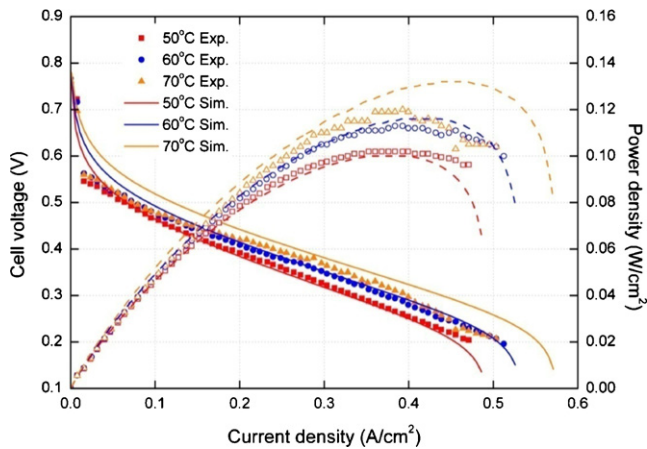
Fig. 7. Comparison of the simulated (lines) and measured (symbols) polarization curves at different cell temperatures (50, 60, and 70 °C) for a methanol concentration of 4 M.

polarization curves at the three different cell temperatures are reduced more in the case of 4 M than in the other cases (of 1–3 M). This implies that for 4 M, the negative effect due to enhanced methanol crossover by the rising temperature becomes comparable with the positive effect that is due to the enhanced electrochemical reaction kinetics and reactant transport with rising temperature (Fig. 7).

The present 1D DMFC model was also validated against the methanol crossover current density data that were measured by Eccarius et al. [12]. Simulated and measured crossover current density curves as a function of the operating current density is presented Fig. 8. It should be noted that the crossover current density can be calculated according to Faraday's law via Eq. (20) as follows.

$$I_{xover} = 6FN_{M,mem} = \underbrace{6n_{d,M}I}_{EOD} + \underbrace{6FD_{M,mem} \frac{c_M^l\big|_{aCL}}{\delta_{mem}}}_{diffusion} \quad (43)$$

The crossover current density is decomposed into the EOD and diffusion components. The conditions for the simulations and experiments are based on a methanol feed concentration of 1.5 M, a
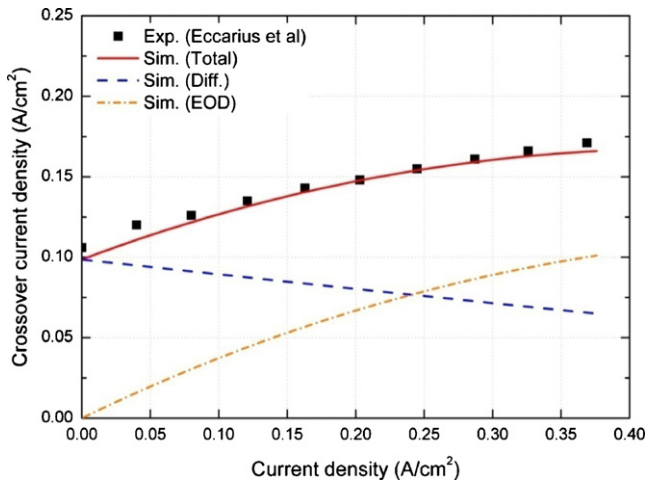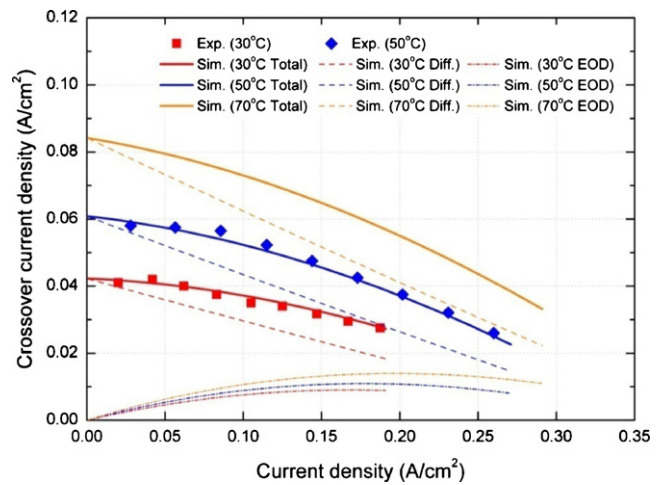

Fig. 8. Simulated (lines) and measured (symbols) methanol crossover current density curves as a function of the cell current density and the contributions of the diffusion and electro-osmotic drag (EOD) to the methanol crossover current density (Nafion 117 with a catalyst loading of 2.5 mg cm^{-2} on both electrodes, 50 °C, 1.5 M solution of methanol, anode flow rate of 3 ml min^{-1}, and the cathode stoichiometry of 6).
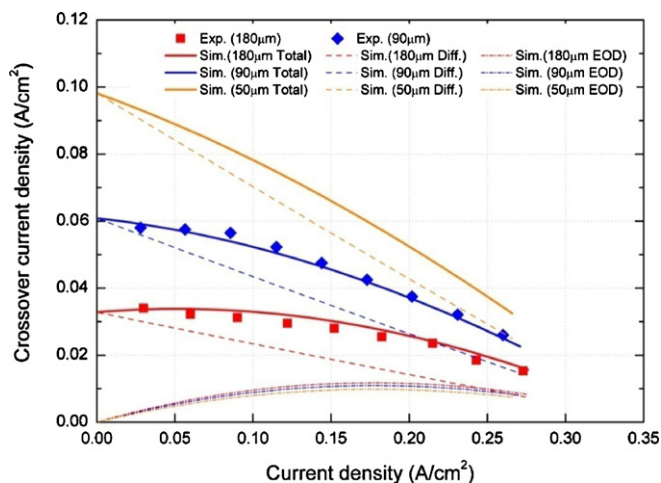

Fig. 9. Simulated (lines) and measured (symbols) methanol crossover current density curves as a function of the cell current density and the contributions of the diffusion and electro-osmotic drag (EOD) to the methanol crossover current density (Nafion 1135 with a catalyst loading of 2.5 mg cm^{-2} on both electrodes, 0.5 M solution of methanol, anode flow rate of 1 ml min^{-1}, and the cathode stoichiometry of 2 for different operating temperatures).

cell temperature of 50 °C, and a Nafion® 117 membrane (180 μm). There is good agreement between the experimental data (symbols) and simulation results (lines); both show an increasing trend with the cell current density. The simulation results further present the contribution of the diffusion and EOD to the total crossover current density. At the OCV, the effect of the EOD is not present and thus, the methanol crossover is fully driven by diffusion. As the operating current density increases, the effect of diffusion continuously decreases because the methanol concentration in the anode catalyst layer is lowered due to the increasing rate of the MOR. On the other hand, according to Eq. (43), the EOD component of the methanol crossover current density continues to increase with cell current density. Therefore, the overall increase in the total crossover current density with increasing cell current density implies that the increasing rate of the EOD component is more dominant than the decreasing rate of the diffusion component under the given conditions.

A comparison of the simulated and measured methanol crossover current densities at the two operating temperatures of 30 and 50 °C is seen in Fig. 9. One more case corresponding to a cell temperature of 70 °C was additionally simulated to investigate the influence of the operating temperature on the methanol-crossover phenomena. All these cases are based on a methanol feed concentration of 0.5 M and a Nafion® 1135 membrane (90 μm). The curves of methanol crossover current density match well across the simulations and experiments and that both the measured and simulated crossover current densities decrease the cell current density, which indicates that the crossover current densities under these conditions are mainly determined by diffusion. In addition, as the cell temperature is elevated, the diffusion component of the crossover current density increases significantly, which illustrates that the diffusion component is the main contributor to the rise in the crossover current density with the temperature. According to the methanol crossover diffusivity correlation, $D_{M,mem}$ in Table 1, it is obvious that the methanol at the anode can more easily diffuse through the membrane at higher cell temperatures.
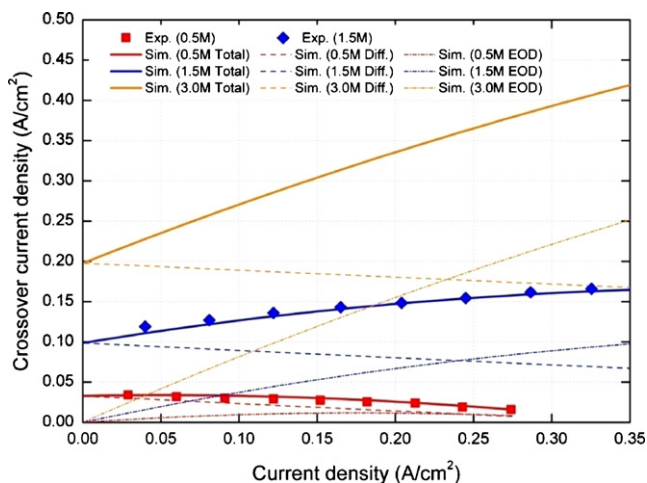
It is expected that the rate of methanol crossover can be affected by the thickness of the membrane. The crossover current density curves simulated with three different membranes, i.e., Nafion® 117 (180 μm), Nafion® 1135 (90 μm), and Nafion® 112 (50 μm),

Fig. 10. Simulated (lines) and measured (symbols) methanol crossover current density curves as a function of the cell current density and the contributions of the diffusion and electro-osmotic drag (EOD) to the methanol crossover current density (a catalyst loading of 2.5 mg cm^{-2} on both electrodes, 50 °C, 0.5 M solution of methanol, anode flow rate of 1 ml min^{-1}, and the cathode stoichiometry of 6 for different membrane thicknesses).

Fig. 11. Simulated (lines) and measured (symbols) methanol crossover current density curves as a function of the cell current density and the contributions of the diffusion and electro-osmotic drag (EOD) to the methanol crossover current density (Nafion 117 with a catalyst loading of 2.5 mg cm^{-2} on both electrodes, 50 °C, anode flow rate of 1 ml min^{-1}, and the cathode stoichiometry of 6 for different methanol feed concentrations).

are presented in Fig. 10. Nafion® 117 and Nafion® 1135, the predicted results can be compared with the experimental data. Again, these crossover current density curves demonstrate good agreement between the results of the simulations and those of the experiments. Also, the results of the simulation model further indicate that the diffusion component of the crossover current density is significantly reduced with thicker membranes, whereas the EOD component remains almost constant, regardless of the membrane thickness.

The final results of validation are presented in Fig. 11 for 0.5 and 1.5 M methanol feed concentrations. Once again, there is excellent agreement in the crossover current density curves between the simulations and experiments for both 0.5 and 1.5 M, and the model successfully captures the experimental trends in the crossover current density under various methanol feed concentrations. In particular, it should be noted that a change in the methanol feed concentration leads to a significant change in the shape of the crossover current density curve, as well as in the degree of methanol crossover. For the 0.5 M case, the crossover current densities are relatively low and decrease with cell current density, whereas the 1.5 M case exhibits higher levels of methanol crossover and an increasing trend in the crossover current density with the cell current density. The detailed simulation results demonstrate that both the EOD and diffusion crossover currents increase significantly as the methanol feed concentration increases. In particular, the EOD crossover current density increases dramatically with cell current density under high methanol feed concentrations which, as seen in Eq. (43), results from increases in both the methanol EOD coefficient, $n_{d,M}$ and the cell current density, I. For the successful use of methanol fuel with high concentration for DMFCs, it is well known that the development of membranes that have greater resistance to methanol crossover is important because the diffusion component of methanol crossover can be significantly reduced by such membranes. Nevertheless, the simulation results in Fig. 11 indicate further that the reduction of the methanol concentration in the anode catalyst layer is even more important in order to suppress simultaneously both the diffusion and EOD components. This reduction can be achieved by designing a highly resistive anode backing layer for methanol transport.

5. Conclusions

The main objective of this study is to compare the simulation results of a 1D DMFC model with experimental data that are measured under a wide range of cell designs and operating conditions. It should be noted that no fitting parameters have been assumed for the comparison activities and that the same model input parameters have been employed for all the cases of comparison. This study mainly involves a comparison of the simulated and measured values for the cell current density data, which were obtained from in-house fuel cell tests and the methanol crossover current density data given by Eccarius et al. [12]. In general, all the comparisons yield excellent agreement under different methanol feed concentrations (1–4 M), cell temperatures (50–70 °C) and membrane thicknesses (90 and 180 μm), which proves the validity and accuracy of the present 1D DMFC model. In addition, a detailed examination is undertaken of the simulation results and experimental data. The trends observed in this study can be summarized as follows.

Both the simulation results and experimental data demonstrate clearly that the operation of a DMFC at a high cell temperature helps to improve cell performance due to the enhanced electrochemical kinetics and the transportation ability of reactants. The beneficial effect of high-temperature operation is diminished, however, when highly concentrated methanol fuel is employed for DMFC operations. The trend is indicative of enhanced methanol crossover flux through the membrane under rising cell temperature.

In the methanol crossover current density profiles, the decrease in methanol crossover density with cell current density can be ascribed to the dominance of the methanol diffusion effect over the EOD effect. On the other hand, the methanol crossover density increases with cell current density when the EOD effect is more dominant. Simulations indicate that the methanol crossover flux through diffusion is sensitive to all the key DMFC design and operating parameters considered in this study. Methanol crossover by diffusion is enhanced under greater methanol feed concentrations and cell temperatures but suppressed under a rising membrane thickness. Unlike methanol diffusion across the membrane, methanol crossover that is driven by the EOD is not altered much with variation in cell temperature and membrane thick-

ness. By contrast, the methanol feed concentration is found to be a significant factor and considerably affects the EOD component of methanol crossover. Therefore, the presented simulation results further indicate that for the use of highly concentrated methanol fuel to increase the specific energy of a DMFC system, both the EOD and diffusion components of methanol crossover should be suppressed, which can be achieved by designing a highly resistive anode backing layer for methanol transport.

Acknowledgement

References

[1] C.E. Shaffer, C.Y. Wang, Handbook of Fuel Cells, vol. 6, John Wiley and Sons, 2009, pp. 749–761.
[2] A. Heinzel, V.M. Barragan, J. Power Sources 84 (1999) 70–74.
[3] X. Ren, T.E. Springer, T.A. Zawodzinski, S. Gottesfeld, J. Electrochem. Soc. 147 (2000) 466–474.
[4] S. Hikita, K. Yamane, Y. Nakajima, JSAE Rev. 22 (2000) 151–156.
[5] M.K. Ravikumar, A.K. Shukla, J. Electrochem. Soc. 143 (1996) 2601–2606.
[6] J.T. Wang, S. Wasmus, R.F. Savinell, J. Electrochem. Soc. 143 (1996) 1233–1239.
[7] K. Scott, W. Taama, J. Cruickshank, J. Power Sources 65 (1997) 159–171.
[8] G. Murgia, L. Pisani, A.K. Shukla, K. Scott, J. Electrochem. Soc. 150 (2003) A1231–A1245.
[9] R. Chen, T.S. Zhao, J. Power Sources 152 (2005) 122–130.
[10] D. Kareemulla, S. Jayanti, J. Power Sources 188 (2009) 367–378.
[11] V.B. Oliveira, D.S. Falcao, C.M. Rangel, A.M.F.R. Pinto, Int. J. Hydrogen Energy 33 (2008) 3818–3828.
[12] S. Eccarius, B.L. Garcia, C. Hebling, J.W. Weidner, J. Power Sources 179 (2008) 723–733.
[13] Z.H. Wang, C.Y. Wang, J. Electrochem. Soc. 150 (2003) A508–A519.
[14] J. Divisek, J. Fuhrmann, K. Gartner, R. Jung, J. Electrochem. Soc. 150 (2003) A811–A825.
[15] W.W. Yang, T.S. Zhao, Electrochim. Acta 52 (2007) 6125–6140.
[16] Y.L. He, X.L. Li, Z. Miao, Y.W. Liu, Appl. Therm. Eng. 29 (2009) 1998–2008.
[17] J. Ge, H. Liu, J. Power Sources 160 (2006) 413–421.
[18] V. Saarinen, O. Himanen, T. Kallio, G. Sundholm, K. Kontturi, J. Power Sources 172 (2007) 805–815.
[19] J. Ko, P. Chippar, H. Ju, Energy 35 (2010) 2149–2159.
[20] P. Chippar, J. Ko, H. Ju, Energy 35 (2010) 2301–2308.
[21] R.B. Bird, W. Stewart, E.N. Lightfood, Transport Phenomena, second ed., John Wiley & Sons Inc., New York, 2002.
[22] W. Liu, The Graduate School Department of Mechanical and Nuclear Engineering. Ph.D. Thesis, The Pennsylvania State University, 2005.
[23] C.Y. Wang, P. Cheng, Int. J. Heat Mass Transfer 39 (1996) 3607–3618.
[24] J.P. Meyers, J. Newman, J. Electrochem. Soc. 149 (2002) A718–A728.
[25] H.A. Gasteiger, N. Markovic, P.N. Ross Jr., J. Caims, J. Phys. Chem. 97 (1993) 12020–12029.
[26] D.M. Bernardi, M.W. Verbrugge, AIChE J. 37 (1991) 1151–1163.
[27] S. Gottesfeld, T.A. Zawodzinski, Advances in Electrochemical Science and Engineering, vol. 5, John Willey & Sons Inc., New York, 1997.
[28] Q. Ye, T.S. Zhao, H. Yang, J. Prabhuram, Electrochem. Solid-State Lett. 8 (2005) A52–A54.
[29] A.A. Kulikovsky, H. Schmitz, K. Wippermann, J. Mergel, B. Fricke, T. Sanders, D.U. Sauer, Electrochem. Commun. 8 (2006) 754–760.
[30] C.E. Shaffer, C.Y. Wang, Electrochim. Acta 54 (2009) 5761–5769.
[31] V. Neburchilov, J. Martin, H. Wang, J. Zhang, J. Power Sources 169 (2007) 221–238.
[32] X. Ren, S. Gottesfeld, J. Electrochem. Soc. 148 (2001) A87–A93.